ACS APPLIED MATERIALS & INTERFACES

Research Article

Cite This: ACS Appl. Mater. Interfaces 2018, 10, 13720−13728

www.acsami.org

Effect of Gallium Substitution on Lithium-Ion Conductivity and Phase Evolution in Sputtered $Li_{7-3x}Ga_xLa_3Zr_2O_{12}$ Thin Films

M. Rawlence,[†,§] A. N. Filippin,[†] A. Wäckerlin,[†] T.-Y. Lin,[†] E. Cuervo-Reyes,[‡] A. Remhof,[‡] C. Battaglia,[‡] J. L. M. Rupp,[§,∥] and S. Buecheler*[,†]

[†]Laboratory for Thin Films and Photovoltaics and [‡]Laboratory Materials for Energy Conversion, Empa—Swiss Federal Laboratories for Material Science and Technology, Überlandstr. 129, CH-8600 Dübendorf, Switzerland

[§]Electrochemical Materials, ETH Zurich, CH-8093 Zurich, Switzerland

[∥]Electrochemical Materials, Massachusetts Institute of Technology (MIT), Cambridge, Massachusetts 02139, United States

Supporting Information

ABSTRACT: Replacing the liquid electrolyte in conventional lithium-ion batteries with thin-film solid-state lithium-ion conductors is a promising approach for increasing energy density, lifetime, and safety. In particular, $Li_7La_3Zr_2O_{12}$ is appealing due to its high lithium-ion conductivity and wide electrochemical stability window. Further insights into thin-film processing of this material are required for its successful integration into solid-state batteries. In this work, we investigate the phase evolution of $Li_{7-3x}Ga_xLa_3Zr_2O_{12}$ in thin films with various amounts of Li and Ga for stabilizing the cubic phase. Through this work, we gain valuable insights into the crystallization processes unique to thin films and are able to form dense $Li_{7-3x}Ga_xLa_3Zr_2O_{12}$ layers stabilized in the cubic phase with high in-plane lithium-ion conductivities of up to 1.6×10^{-5} S cm^{-1} at 30 °C. We also note the formation of cubic $Li_7La_3Zr_2O_{12}$ at the relatively low temperature of 500 °C.

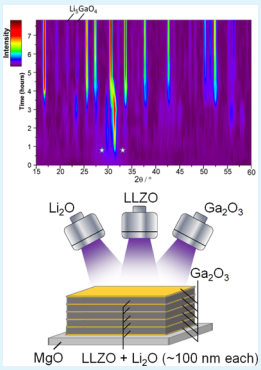

KEYWORDS: *solid-state electrolyte, LLZO, thin-film LLZO, sputtering*

1. INTRODUCTION

The $Li_7La_3Zr_2O_{12}$ (LLZO) garnet has been proposed as a promising candidate for the electrolyte in all-solid-state lithium-ion batteries.[1] It exists in three-phase polymorphs, one tetragonal arrangement with space group $I4_1/acd$ (no. 142) (ref 2) and a lithium-ion conductivity of up to ∼1.1×10^{-4} S cm^{-1} at room temperature (RT) (ref 3), and two cubic modifications, the more commonly known space group $Ia\bar{3}d$ (no. 230) (ref 4) and the recently discovered $I4\bar{3}d$ (no. 220) (ref 5). The cubic phases have higher lithium-ion conductivities but are not stable at room temperature (RT). The cubic phase can be stabilized at RT through the addition of certain elements on the lithium, lanthanum, or zirconium structural sites. Originally achieved through Al^{3+} substitution on the lithium site, a lithium-ion conductivity of 4×10^{-4} S cm^{-1} was obtained for the $Ia\bar{3}d$ space group.[6] Since then, a large variety of elements have been used to stabilize the highly conductive cubic phase and increase the lithium-ion conductivity.[7−18] Co-alloying with two or more elements has also been explored usually by substituting Al^{3+} or Ga^{3+} on the Li^+ site in addition to a substitution on the La^{3+} or Zr^{4+} site for the garnet.[19−25] The RT ionic conductivity of Ga-doped LLZO pellets has been shown by several research groups to reach above 1×10^{-3} S cm^{-1}, with between 0.20 and 0.25 Ga per unit cell.[5,26,27] It has also been shown that adding Ga metal to presynthesized LLZO particles helps to reduce the sintering temperature and induces a phase change at temperatures as low as 600 °C.[28] Fe-doped LLZO has recently been reported with a similar bulk ionic conductivity of 1.38×10^{-3} S cm^{-1}.[29] In addition to favorable lithium-ion conductivity, LLZO shows indications of intrinsic stability vs lithium metal. Because of its wide electrochemical stability window, the use of low-voltage anodes and some high-voltage cathodes is possible, leading to cells with both high voltage and energy densities.[30] Interfacial resistance, wetting properties, and chemical stability can also be significantly improved with a silicon or Al_2O_3 interlayer.[31,32]

By reducing the electrolyte thickness from pellet to thin films, the proportion of electroactive material in the battery is increased. Although lithium-ion conductivities of liquid electrolytes[33] are generally higher with ionic conductivities of up to 1×10^{-2} S cm^{-1}, the internal resistance of solid-state batteries could still be lower due to the 2 orders of magnitude decreased electrolyte thickness when compared with liquid-type cells that require a separator in the range of 12−40 μm as a necessary component.[34] Interfacial resistances between electrolyte and cathode can also be decreased with the addition of interlayers, such as $LiNbO_3$[35] and $LiAlO_2$,[36] which prevent side reactions during synthesis and battery operation. However, until now there has been little progress toward the integration of LLZO thin films into batteries. The primary reason for this has been the difficulty in processing dense, crack-free, and phase pure LLZO films with

Received: February 23, 2018
Accepted: April 2, 2018
Published: April 2, 2018

DOI: 10.1021/acsami.8b03163
ACS Appl. Mater. Interfaces 2018, 10, 13720−13728

lithium-ion conductivity comparable to that of the bulk material. Several attempts have been made to deposit thin films of LLZO with various techniques, such as pulsed laser deposition (PLD),[37−41] magnetron sputtering,[42,43] aerosol-assisted deposition,[44] sol−gel deposition,[45−47] and metal−organic vapor deposition (MOCVD).[48] The type of method used has clear implications on the microstructure, phase content, and ultimately the lithium-ion conductivity of the resulting film. For example, sol−gel deposition allows the stoichiometry to be controlled and therefore the lithium loss that occurs during high-temperature processing can be compensated for; however, the density of the resultant film is often poor with a porous microstructure.[49,50] Katsui and Goto achieved stabilized high-purity thin films of cubic LLZO by actively controlling the lithium flow during deposition using MOCVD.[48] The granular growth and the required high substrate temperatures above 800 °C make it challenging for integration into devices. Physical vapor deposition methods such as magnetron sputtering or PLD result in a higher film density, but lithium loss during deposition remains a challenge, resulting in lithium-deficient films that tend to form the nonconductive pyrochlore phase, $La_2Zr_2O_7$, more easily upon crystallization.

In this work, we present the radio-frequency magnetron cosputtering approach that allows to actively compensate for lithium losses and to control the addition of phase stabilizing elements. With simultaneous cosputtering from ceramic LLZO and Li_2O targets, we obtain Li-stuffed LLZO thin films. To stabilize the highly conductive cubic LLZO phase, lithium was partially substituted by gallium atoms through multilayer depositions of LLZO + Li_2O/Ga_2O_3, followed by annealing in controlled ambient. In situ X-ray diffraction (XRD) during the postdeposition annealing on thin films with a range of varied Ga concentrations provides a detailed view of the crystallization processes from amorphous state in the as-deposited film into cubic-phase polycrystalline LLZO. Here, we contribute to the fundamental understanding of how Ga concentration affects phase formation and stability of LLZO thin films. These results indicate that crystallization of cubic LLZO already can start at temperatures as low as 500 °C. This finding has strong implications on the materials and design of thin-film batteries. The effect of tailoring the Ga concentration on the lithium-ion conductivity is investigated by impedance spectroscopy at different temperatures. Non-Arrhenius behavior of the ionic conductivity is observed, and its origin is discussed. Finally, conclusions on the role of gallium in the structure formation and stabilization of cubic LLZO structures are presented, which serve as engineering guidelines to design future solid-state batteries.

2. EXPERIMENTAL SECTION

2.1. Preparation of Solid-State Electrolyte Thin Films by Cosputtering. Radio-frequency (RF) magnetron sputtering equipment (Orion sputtering system, AJA) with five cathodes in confocal off-axis geometry was used for growth of the thin films. Sputtering targets composed of Li_2O (3 N, 90% density), $Li_7La_3Zr_2O_{12}$ (3 N, 90% density), and Ga_2O_3 (4 N, 90% density) mounted on Cu backing plates were used from TOSHIMA Manufacturing Co., Japan. The MgO (Crystec, single crystal (100), 10 mm × 10 mm) substrates were precleaned using Ar plasma etching with a substrate bias of 20 W for 2 min. Reference films were deposited from the LLZO target without intentional substrate heating (the monitored substrate temperature did not exceed 50 °C during deposition). Lithium-stuffed LLZO films were obtained by simultaneous cosputtering from LLZO and Li_2O targets. The deposition rates from the individual targets were measured before the film growth using a quartz crystal microbalance positioned where the substrate would be during deposition. During deposition, constant rates are assumed. The deposition rates are adjusted to a ratio of 1 mol of LLZO per 4 mol of Li_2O. The following deposition parameters were used: 25 sccm Ar flow, process pressure 50 mPa, working distance of 11.8 cm, Li_2O target power density 5 W cm^{-2}, and LLZO target power density 2.5 W cm^{-2}.

The addition of various amounts of Ga into the film was achieved through multilayer deposition of LLZO + Li_2O and Ga_2O_3 with a total of six layer sequences, as shown in Figure 1. The targeted gallium concentrations (x_{Ga}) in the compound $Li_{7-3x}Ga_xLa_3Zr_2O_{12}$ were x_{Ga} = 0.2, 0.18, 0.16, and 0.14. The thickness of the six Ga_2O_3 interlayers was varied for the targeted Ga concentrations. The proportion of Li_2O in the cosputtered layer was adjusted taking into account the added amount of Ga_2O_3 to obtain stoichiometry. The nominal composition of each film was calculated on the basis of quartz crystal microbalance rate measurements prior to depositions. The Ar flow rate and pressure were kept constant (25 sccm and 50 mPa, respectively), and the power density used for Ga_2O_3 deposition was 3 W cm^{-2}.

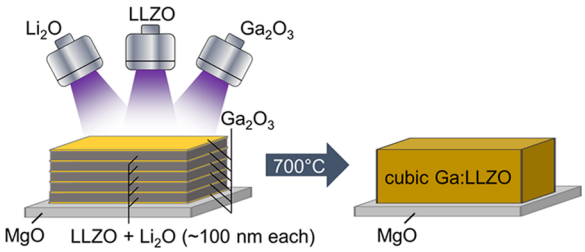

Figure 1. Schematic of method for forming thin-film gallium-doped LLZO based on multilayer cosputtering and a post-annealing process.

2.2. Characterization of Crystalline Microstructure and Ionic Conductivity. The amorphous films deposited at RT were placed in an Anton Paar XRK 900 reaction chamber with Be windows for heating the samples up to 700 °C, measured via thermocouple, under a flow of 50 sccm O_2. During the heating, in situ grazing incidence X-ray diffractograms were obtained using a PANalytical X'Pert[3] powder diffractometer using a Cu Kα wavelength at an accelerating voltage of 35 keV with grazing incidence geometry and an incidence angle of 1°. Post-annealing measurements were carried out using the same tool and parameters but with a longer scan time. Contour plots were compiled using grazing incidence X-ray diffraction (GI-XRD) data smoothed by the adjacent averaging method to reduce noise in the low-intensity regions. Lattice constants were calculated from the peak positions of the XRD diagrams using Rietveld refinement. X-ray photoelectron spectroscopy (XPS) was utilized to identify atomic concentrations in the LLZO film, as well as to assign corresponding chemical states of the elements. The measurements were carried out at RT with monochromatized Al Kα X-ray source (PHI Quantum 2000) on LLZO with the different Ga concentrations. To obtain a high number of counts for low elemental concentrations, the spectra were acquired with 117.4 eV pass energy, where the full width at half-maximum (FWHM) is ∼1.8 eV. The X-ray spot size was 150 μm. Sputter depth-profiling was necessary to obtain a more accurate representation of the bulk properties of the film, as surface layers are known to form upon contact with air, such as Li_2CO_3. Sputtering was done using an Ar^+-ion sputter gun, at an acceleration voltage of 2 kV and total sputtering time of 45 min. The spectra for quantification of the films were selected from the middle of each film, where the signals for La and Zr are either at a maximum or in the middle of a plateau; see Figure S5. The effects of preferential sputtering and forward sputtering may change the stoichiometry of the film surface. In addition, the matrix effect for each element in LLZO is not known; however, a valid comparison between measured elemental signals can be made under the assumption that the matrix effects are similar for each film. Therefore, the values presented from XPS analysis are not absolute values and only relative comparison is valid. The error is estimated to be in the order of ∼10%. Spectra were fitted with

DOI: 10.1021/acsami.8b03163
ACS Appl. Mater. Interfaces 2018, 10, 13720−13728

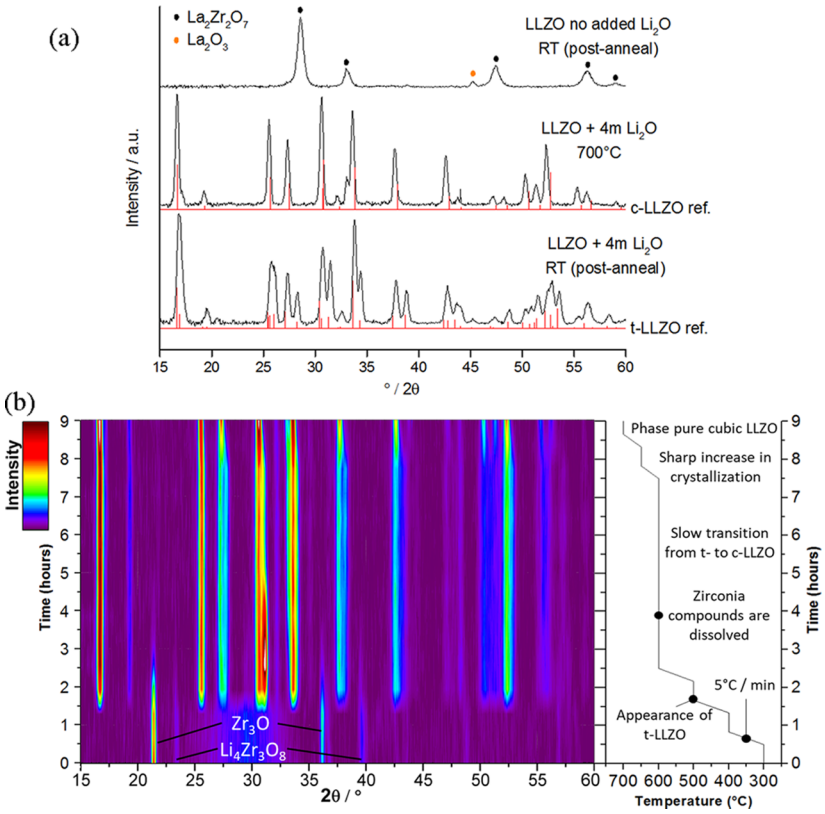

Figure 2. (a) XRD of LLZO film with no additions after annealing at 700 °C compared with film cosputtered with Li_2O XRDs at 700 °C in situ and then pos-tannealing. Reference patterns for cubic and tetragonal LLZO are from the ICSD database, (ICSD 422259) and (ICSD 246817), respectively. (b) Phase evolution of cosputtered film LLZO + Li_2O, showing transition from tetragonal LLZO to cubic LLZO at 600 °C. To the right is the temperature−time profile of the annealing process with phase annotations. The ramp rate for heating/cooling was 5 °C min^{-1}.

Gaussian−Lorentzian mixed function, and atomic concentrations were evaluated using empiric relative sensitivity factors of the equipment.

In-plane electrochemical impedance spectroscopy (EIS) was performed using a Zahner (IM6) impedance bridge with a Linkam stage (HFS-600E, U.K.) containing a two-point probe electrode geometry of gold-coated tungsten tips. Measurement parameters included an alternating current voltage of 50 mV, a frequency range between 1×10^6 and 0.1 Hz, and a flow of 50 sccm synthetic air to prevent reactions with moisture and CO_2 that are known to occur with LLZO.[51] Temperature was measured with a thermocouple in contact with the substrate surface. Au top contacts with 100 nm thickness, 7.5 mm width, and a separation of 250 μm were deposited via thermal evaporation. Zview was used for data processing, including data validation using the Kramers−Kronig test. To ensure reliability of the data, measurements were carried out over several heating/cooling cycles. The first heating/cooling cycle yielded large differences in conductivity depending on whether the sample was being heated or cooled. Performing further cycles under the same conditions resulted in more consistent results; therefore, the data for the quantitative analysis was extracted from the second cooling step for all films.

3. RESULTS AND DISCUSSION

3.1. Lithium Lanthanum Zirconate Thin Films Cosputtered with Lithium Oxide. As-deposited films prepared by RF-magnetron cosputtering from LLZO and Li_2O targets reveal an amorphous structure (see GI-XRD measurement in the Supporting Information Figure S1). After deposition of the films at RT and annealing at 700 °C for 2 h, the films prepared without the extra addition of Li from a Li_2O target crystallized directly into the lithium-free $La_2Zr_2O_7$ phase, as shown in Figure 2a (top pattern). The addition of extra lithium from the Li_2O target promoted the formation of the cubic LLZO phase (ICSD 422259) while dwelling at 700 °C during the annealing phase (Figure 2a middle pattern). No secondary binary or ternary lithium-free phases are detected in such prepared films. After cooling the sample to RT, the structure reverted back to the tetragonal LLZO phase (ICSD 246817), as illustrated in Figure 2a in the bottom pattern. This transition back to tetragonal LLZO is expected to occur as there is no element added to stabilize the cubic phase at RT.[52]

The phase evolution during annealing of the film prepared by cosputtering from LLZO and Li_2O targets is presented in Figure 2b in an intensity contour plot made from a compilation of GI-XRD data. The corresponding temperature−time profile of the annealing process is shown on the right hand side. The contour plot starts at 300 °C, and the temperature is increased in 100 °C intervals with a dwell time of 1 h at each step for GI-XRD measurements to observe possible changes in the crystal structure. At 300 °C, some crystalline material had already formed that could indicate the formation of $Li_4Zr_3O_8$ (JCPDS 01-041-0324) and Zr_3O (JCPDS 01-074-1282), although not enough peaks are present for a clear assignment. A comparison of this diffractogram with the two reference patterns is shown in Figure S2. A broad reflection is also observed centered around 2θ of 30°, signifying that some portion of the film is still amorphous. Upon annealing to a temperature of 500 °C, additional peaks are measurable that can all be ascribed to the tetragonal LLZO phase. A maximum intensity of the peaks corresponding to the tetragonal phase of LLZO is measurable upon reaching 600 °C. During the dwelling period at 600 °C, the peaks corresponding to cubic LLZO gradually increase in intensity until the 3 h mark after which no further changes occur, signifying

DOI: 10.1021/acsami.8b03163
ACS Appl. Mater. Interfaces 2018, 10, 13720−13728

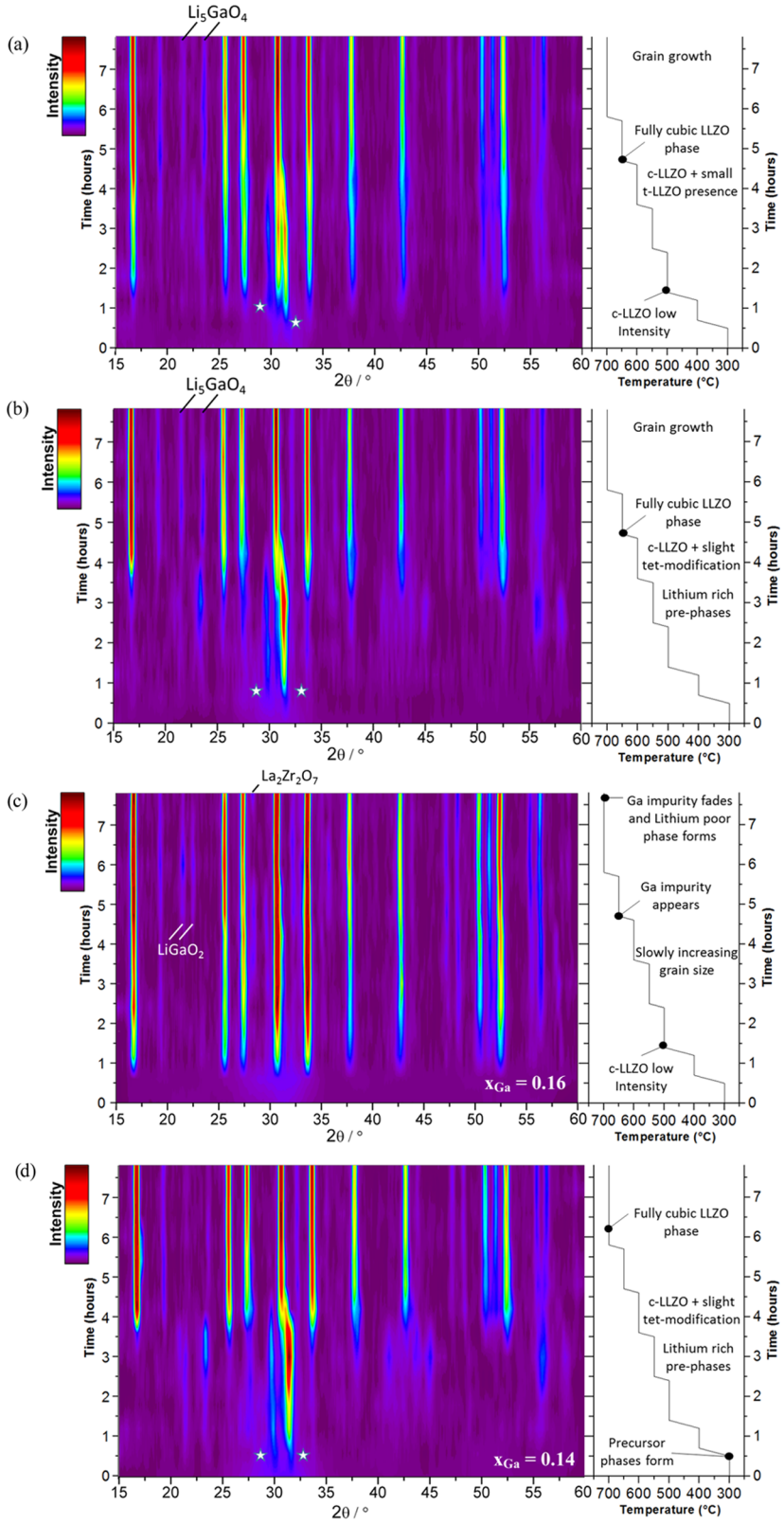

Figure 3. Phase evolution of films with Ga concentrations of (a) 0.20 Ga, (b) 0.18 Ga, (c) 0.16 Ga, and (d) 0.14 Ga with annotated temperature profiles to the right. All films crystallize into the cubic phase at >600 °C. The star symbol is to label precursor phases with tentative assignment to ZrO_2.

that equilibrium between both phases is reached. Further annealing to 650 °C results in cubic LLZO dominating as the primary phase, and by 700 °C, a complete transition from tetragonal to cubic phase has occurred.

3.2. Gallium Alloying of Lithium Lanthanum Zirconate Thin Films Cosputtered with Lithium Oxide. To dope the structure with Ga, six interlayers of Ga_2O_3 were sputtered in between the LLZO + Li_2O films at RT. Four multilayer stacks with varying Ga_2O_3 layer thicknesses were deposited, targeting

DOI: 10.1021/acsami.8b03163
ACS Appl. Mater. Interfaces 2018, 10, 13720−13728

the nominal gallium concentrations (x_{Ga}) in the compound $Li_{7-3x}Ga_xLa_3Zr_2O_{12}$ of x_{Ga} = 0.2, 0.18, 0.16, and 0.14. In the following, the films with different Ga concentrations are labeled according to the nominal (targeted) composition. As the post-annealing process for each film proceeds, XRD is carried out periodically and converted into intensity contour plots shown in Figure 3a−d. An altered temperature profile is used that rises to 500 °C quickly then dwells for an hour at each subsequent 50 °C step up to 700 °C, as shown in the temperature profiles to the right of each figure.

For all Ga-doped films, there were no diffraction peaks recorded at RT and diffraction peaks start to emerge at 300 °C. From this point onward the crystallization process differs between each film with different nominal Ga contents, which we will discuss in detail through the following:

3.2.1. Ga:LLZO Thin Film with x_{Ga} = 0.20. In the GI-XRD diagram of the LLZO film with x_{Ga} = 0.20 (Figure 3a), the first peak is observed at 400 °C at 2θ = 31.5°. This peak indicates the formation of ZrO_2 with a baddeleyite structure type (JCPDS 00-037-1484); however, it must be noted that lack of additional peaks does not allow unambiguous assignment. At 500 °C, the main peaks of the cubic LLZO are already clearly visible at 16.8°, 25.8°, 27.7°, 31°, 34°, 38.2°, and 43.2° and further three peaks between 50° and 54°. In addition, a peak at 29.8° appears that could be assigned to the ZrO_2 (101) peak (JCPDS 01-079-1763). Upon reaching 600 °C, the diffraction peaks of the intermediate phases begin to fade. At this temperature, tetragonal LLZO is also formed, which can be most clearly observed in the partial splitting of the peak at 37.8° and the triple peaks between 50° and 54° becoming more broad; a conventional XRD is shown in Figure S3 to highlight this development. Heating to 650 °C causes the secondary phase peaks at 29.8° and 31.5° to fully disappear, whereas the LLZO peaks intensify and a complete transition to the cubic phase takes place. Additional peaks with low intensity at 23.6° and 21.5° become visible, which fit well to the Li_5GaO_4 phase (JCPDS 00-024-0613). The final annealing step at 700 °C caused a further increase in peak intensities of the cubic LLZO phase, indicating ongoing grain growth.

3.2.2. Ga:LLZO Thin Film with x_{Ga} = 0.18. Figure 3b shows the phase evolution for the Ga:LLZO thin film with x_{Ga} = 0.18. Similarly, as in the previous case, peaks at 29.8° and 31.5° that indicate ZrO_2 formation appear at 400 °C. However, no further changes take place until 550 °C, where a combination of peaks appear that originate from several precursor phases, including $La_4Ga_2O_9$, Li_4ZrO_4, and Li_5GaO_4. At 600 °C, all diffraction peaks of the ternary intermediate phases fade and LLZO starts to form into the cubic phase with some tetragonal LLZO peaks visible in the broadening of peaks between 50° and 54° and some splitting in the peaks at 38.2° and 43.2°. At 650 °C, the full transition to LLZO to the $I4\bar{3}d$ cubic phase occurs with a small secondary phase peak at 23.6° that may correspond to Li_5GaO_4. At 700 °C, there is an increase in peak intensities, indicating grain growth.

3.2.3. Ga:LLZO Thin Film with x_{Ga} = 0.16. The Ga:LLZO layer with x_{Ga} = 0.16 directly crystallizes into cubic LLZO at 500 °C (Figure 3c). No intermediate crystalline material or phase is observed. All peaks corresponding to cubic LLZO undergo continuous increases in intensity as the temperature increases. At 700 °C, there is appearance of peaks at 21.5° and 22.5°, likely corresponding to $LiGaO_2$ (ICSD 01-072-1640). These peaks become lower in intensity during the dwell at 700 °C, signaling a possible absorption of Ga into the LLZO crystal structure. Toward the end of the dwell, at 700 °C, an additional peak at 28° begins to appear that matches the primary peak of the lithium-deficient $La_2Zr_2O_7$ phase (ICSD 01-075-0346); this indicates that lithium loss is occurring.

3.2.4. Ga:LLZO Thin Film with x_{Ga} = 0.14. This layer shows a similar phase evolution as with x_{Ga} = 0.18, the late crystallization of LLZO at 600 °C, and the same intermediate phases forming at 550 °C (Figure 3d). The only significant difference is the lower quantity of Ga-containing secondary phases in the final XRD at 700 °C.

The RT GI-XRD pattern for each film after annealing up to 700 °C is shown in Figure 4 together with the LLZO layer

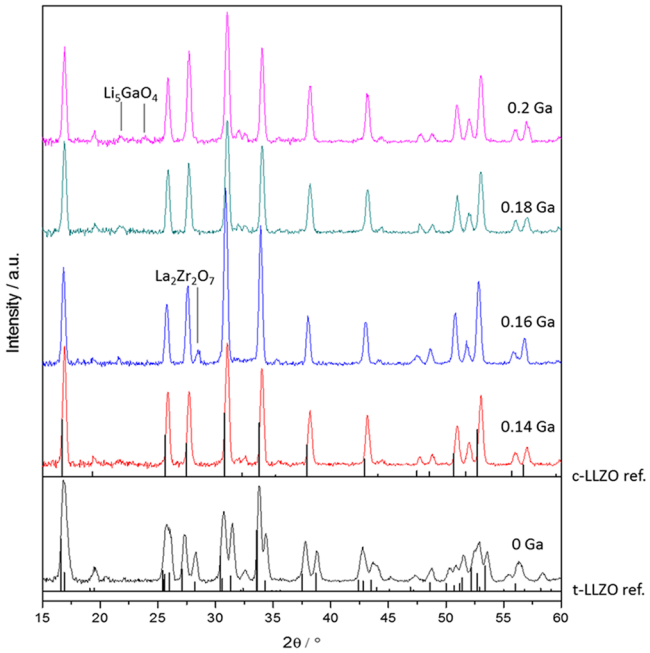

Figure 4. RT XRD of thin films after thermal treatment with varying contents of Ga and Li. Reference patterns for cubic and tetragonal LLZO are from the ICSD database, (ICSD 422259) and (ICSD 246817), respectively.

without addition of Ga. A comparison between the Ga-containing and Ga-free films shows the clear effect of Ga on the stabilization of the cubic phase at RT. The layer with x_{Ga} = 0.16 shows a slightly preferred orientation with greater relative intensity for the two peaks between 30° and 35°, corresponding to the (420) and (422) planes of cubic LLZO phase. The corresponding Lotgerig factors are 0.09 and 0.06, respectively.[53] The lattice parameters, derived from Rietveld refinement, for each film from x_{Ga} = 0.20−0.14 are 12.953, 12.954, 12.989, and 12.954 Å, respectively. These values are lower than the previously obtained value of 12.971 Å for 0.25 Ga substituted bulk LLZO pellets[5] with the exception of x_{Ga} = 0.16, which is higher for unknown reasons. The difference between these values may be explained by thermally induced stresses due to the different coefficients of thermal expansion of the film and the substrate or microstrain. SEM of film surface and cross sections for x_{Ga} = 0.20−0.14 are shown in Figure S4a−d, respectively.

Although the XRD pattern that formed is not influenced by the different Ga contents within this range, the phase evolution, particularly in the temperature range from 300 to 600 °C, showed a strong dependence.

Now, to probe the chemical composition, XPS depth profile measurements were conducted on the same films after the annealing at 700 °C and a representative XPS scan taken from the

DOI: 10.1021/acsami.8b03163
ACS Appl. Mater. Interfaces 2018, 10, 13720−13728

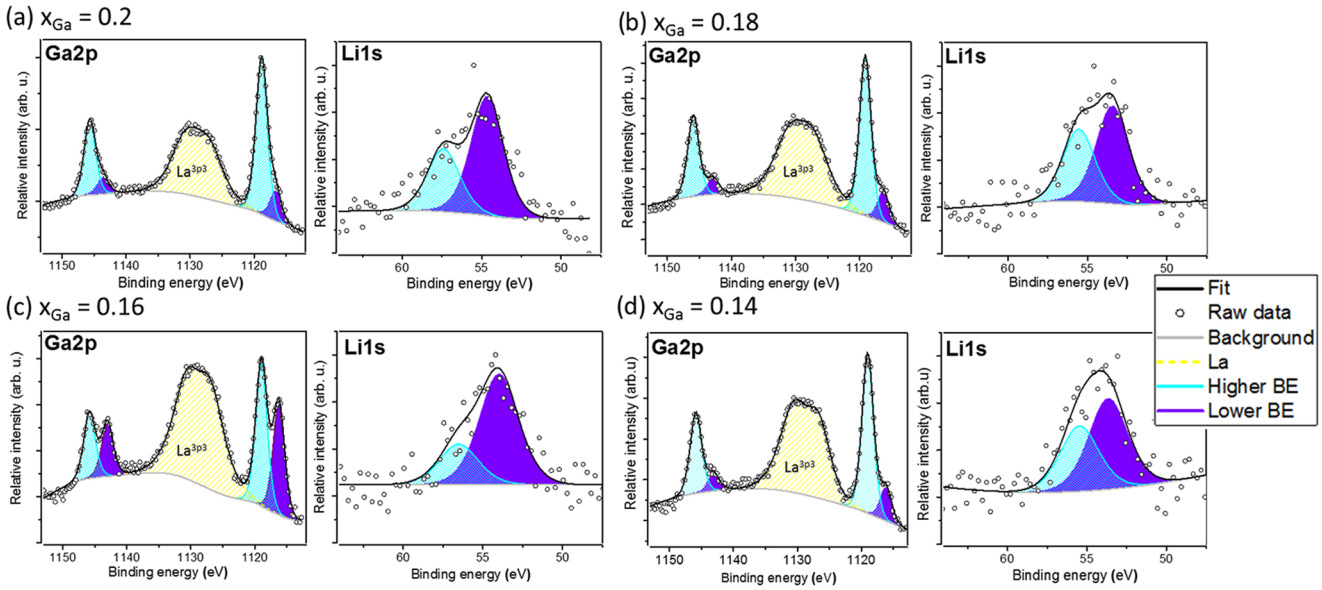

Figure 5. XPS spectra of Ga 2p and Li 1s orbitals for gallium-doped samples of (a) 0.20 Ga, (b) 0.18 Ga, (c) 0.16 Ga, and (d) 0.14 Ga. Two bonding environments are observed for both elements, indicating the presence of a second phase in the thin films. The outlier point in the Li 1s spectrum in (a) is later removed for an improved fit, as described in Table 1.

Table 1. Relative Elemental Concentrations, as Calculated by XPS, for Each Sample with Nominal Ga Contents between 0.20 and 0.14[a]

			predicted x_{Ga}			
element	orbital	BE (eV)	x_{Ga} = 0.2[b]	x_{Ga} = 0.18	x_{Ga} = 0.16	x_{Ga} = 0.14
Ga	$2p_{3/2}$	1116.7	0.24	0.23	0.58	0.2
	$2p_{3/2}$	1119.0	1.23	1.16	0.73	0.97
		total	1.47	1.39	1.31	1.17
Li	1s	53.9	8.32/5.54	5.01	6.85	5.35
	1s	56.2	4.41/3.15	3.70	2.52	3.86
		total	12.73/8.64	8.71	9.37	9.21
Zr	$3d_{5/2}$	total	2.42	2.08	2.28	2.19
La	$3d_{5/2}$	total	3	3	3	3

[a]Values are normalized around La content, which is set to 3 for each sample for comparison to the expected formula: $Li_7La_3Zr_2O_{12}$. [b]Removing the outlier point over the Li 1s peaks in Figure 5a results in lower lithium values for both BEs.

center of each film where relative La and Zr contents reach a maximum plateau, as illustrated in Figure S5. All XPS spectra were charge corrected with respect to the La $3d_{5/2}$ photoelectron line position for La_2O_3 at 835.1 eV (CAS registry number 1312818).

The Ga 2p level contains two doublets, one with lower binding energies (BEs) of 1116.7 eV for the $2p_{3/2}$ and 1143 eV for the $2p_{1/2}$ photoelectron line position and a more dominant one with a shift of +2.3 eV having a $2p_{3/2}$ line at 1119 eV and $2p_{1/2}$ line at 1145.3 eV; see Figure 5. On the basis of the maximum saturation of Ga in the LLZO lattice being in the region of 0.5 Ga per LLZO,[5,54] the minor doublet can be assigned to the Ga−O bond in the LLZO lattice and the dominant doublet to the Ga−O bond in either $LiGaO_2$, which is observed via XRD, or an amorphous, Ga-rich phase, which is expected to precipitate at the grain boundaries of LLZO.[28] Figure 5 also shows the Li 1s signals for the four samples. Fitting the minimum number of peaks with a fixed FWHM of 2 eV resulted in two different bonding energies at 53.9 and 56.2 eV. There is no overlap of Li 1s with Mg peaks from the substrate as no Mg was detected at this depth. The spectra and corresponding fits used for quantification of La $3d_{5/2}$, Zr $3d_{5/2}$, and O 1s can be found in Figure S6. In Table 1, the four different Ga concentrations, as estimated from the quartz crystal microbalance, are compared to the elemental values determined by XPS. Errors in the elemental concentration between different binding energies are expected to be in the order of 10% when operating at high-pass energies of 117.4 eV. There is a relatively higher proportion of Ga in all films; however, an overall trend of decreasing gallium content from films x_{Ga} = 0.20−0.14 is still observed.

By plotting the concentrations derived from the two components at lower BE for Li and Ga for each sample, certain trends may be seen, as shown in Figure S7. The lower BE components of Li and Ga correlate well across all samples; therefore, the 53.9 eV Li 1s peak can be assigned to LLZO. The higher BE components also correlate well, indicating that they belong to the same chemical compound that could be an amorphous secondary phase. Relative to the apparent Ga content in the films, the Li content is lower than expected. This may be caused by the presence of O^{2-} vacancies, each of which result in the loss of two Li^+ from the structure. The presence of oxygen vacancies in LLZO was recently proven by Kubicek et al.[55] There is currently no explanation for why the Ga content in the LLZO was not at its limit for all films despite its overall abundance. The

DOI: 10.1021/acsami.8b03163
ACS Appl. Mater. Interfaces 2018, 10, 13720−13728

most notable connection linking the early crystallization of LLZO and the chemical content of the films is the relatively higher lithium and gallium contents of the x_{Ga} = 0.20 and 0.16 films.

3.3. Electrochemical Impedance Spectroscopy Analysis of Lithium Lanthanum Zirconate Thin Films. Impedance spectroscopy carried out over three heating/cooling cycles was employed to determine the (in-plane) ionic conductivity of the annealed thin films. Discrepancies over the course of three heating cycles are shown in Figure S8. The Kramers–Kronig test[56] was carried out for all temperatures to verify the self-consistency of the impedance data, an example of which is shown for x_{Ga} = 0.18 in Figure S9. The direct current conductivity was extracted from both the impedance and the electric modulus plot to check for consistency and to ensure that surface effects are not affecting our estimations; examples are shown in Figure 6. A comparison of the conductivity values extracted over the full temperature range from the two methods is shown in Figure S10.

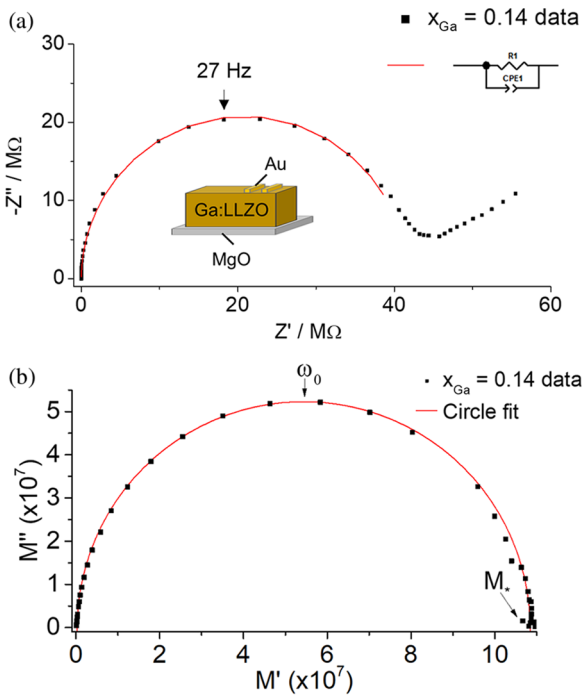

Figure 6. (a) Nyquist plot for electrochemical impedance spectroscopy (EIS) measured at 50 °C for LLZO film with 0.14 Ga, resulting in a conductivity of 1.6×10^{-5} S cm^{-1}. An R-CPE equivalent circuit model is used to fit the data. (b) Plot of the complex electric modulus of the same film with key variables for calculating ionic conductivity labeled.

The conductivities for the Ga-doped films at RT for x_{Ga} = 0.20, 0.18, 0.16, and 0.14 are 1.2×10^{-6}, 2.7×10^{-6}, 6.9×10^{-7}, and 3.0×10^{-6} S cm^{-1}, respectively. Comparing these results to the XPS-measured elemental compositions, it appears that higher levels of Ga in the LLZO may cause lower conductivities at RT. The initial measurement of film x_{Ga} = 0.14, before high-temperature measurements were carried out, as shown in Figure 6, yielded a conductivity of 1.6×10^{-5} S cm^{-1}, although the conductivity quickly degraded with successive measurements in O_2 atmosphere before stabilizing at almost 1 order of magnitude lower. This initial value for polycrystalline cubic LLZO was comparable to what has been obtained for epitaxially grown LLZO thin films.[37]

The temperature dependence of the conductivity is shown in Figure 7 over the range from 400 °C to RT. A smooth deviation

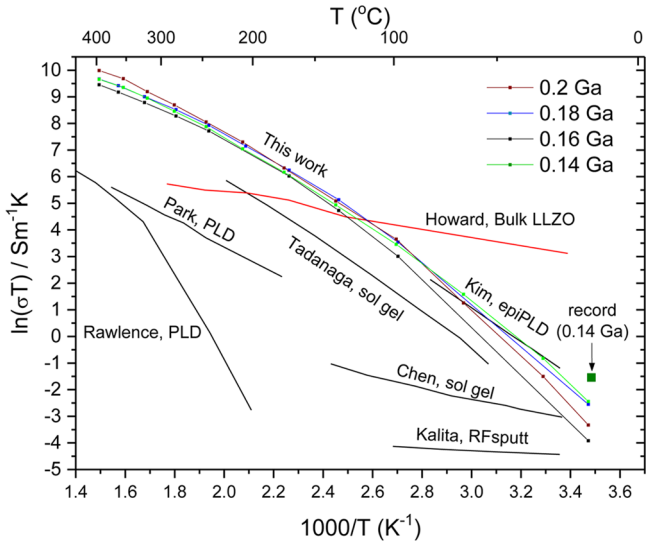

Figure 7. Arrhenius-type plot for LLZO films with 0.20, 0.18, 0.16, and 0.14 Ga concentrations. Initial high conductivity measurement of 0.14 Ga film shown in Figure 6a is plotted as a single point. Other reference data for thin-film LLZO from the literature were Kim et al.,[37] Rawlence et al.,[39] Park et al.,[40] Kalita et al.,[42] Tadanaga et al.,[45] and Chen et al.[46] Howard et al.[54] show data obtained from a pellet of LLZO doped with 0.5 Ga per unit cell.

from the Arrhenius behavior is observed for all investigated samples, with the plot of conductivity on the logarithmic scale vs inverse of temperature not being a straight line. The increase of the activation energy (the slope) as the temperature is decreased is a commonly observed feature in ionic conductors. Generally, the first approach for interpreting such a feature is to fit the curve to an appropriate number of activation energies that represent different conductivity mechanisms in the material. In this case, the data was fit with two activation energies using the general expression from linear response theory over the full temperature range, as described in the Supporting Information, which gives us apparent activation energies $E_1 = 0.66 \pm 0.03$ eV and $E_2 = 0.38 \pm 0.03$ eV. Although the data can be fit this way, it is unclear which conductivity mechanism would yield an activation energy of 0.66 eV in LLZO. On the other hand, E_2 matches well with the expected value for bulk LLZO lithium-ion conductivity.[27] Further analysis of the physical implications of this approach (presented in detail in the Supporting Information) shows that there is a strong mismatch of 1.28×10^4 in the ratio between the jump-attempt frequencies connected to E_1 and E_2. Both these values should be close to the lattice vibrations (normally $\sim 10^{15}$ Hz). The ion–ion correlation effect is capable of explaining deviations from the Arrhenius behavior; we refer here to ref 57 for details. It was also used in relation to crystalline lithium-ion conductors.[58] By fitting the data with the coupling model (see in the Supporting Information) that makes use of a single temperature-independent activation energy, which is determined by the lattice energy barriers, a value of $E_a = 0.35 \pm 0.02$ eV is obtained. In Figure S10, the temperature dependence of the effective activation energy due to correlation effects is presented in further detail.

DOI: 10.1021/acsami.8b03163
ACS Appl. Mater. Interfaces 2018, 10, 13720−13728

4. CONCLUSIONS

Herein, we demonstrate cosputtering followed by post-annealing as a promising approach for the formation of cubic-LLZO thin films with high lithium-ion conductivity and thermal stability. Importantly, the issue of lithium loss during vacuum deposition and annealing is overcome by gaining control over the initial lithium content in the film. By incorporating Ga_2O_3 interlayers, the cubic phase is stabilized at RT with an initial lithium-ion conductivity of 1.6×10^{-5} S cm^{-1} at RT, which degrades down to 3.0×10^{-6} S cm^{-1} during high-temperature conductivity measurements. Non-Arrhenius behavior was observed over a large temperature range and was modeled and discussed with the approach of the two-activation-energy model as well as an ion−ion correlation model.

Through studying the effect of gallium content on phase evolution during annealing, a more in-depth understanding of the interplay between the precursor phases and desired LLZO phases has been gained, particularly in the case of LLZO with high Ga content. In the lower temperature region of the annealing process between 300 and 600 °C, the effect of the Ga content on the crystallization was particularly pronounced. The $x_{Ga} = 0.16$ and 0.20 films, with XPS-measured Ga contents of 0.58 and 0.24, respectively, formed a low-temperature cubic LLZO phase at 500 °C, whereas films with lower Li and Ga contents formed LLZO at 600 °C. Synthesis of the desired cubic phase at these lower temperatures is of particular interest for later integrating such films into a full solid-state cell.

■ ASSOCIATED CONTENT

Supporting Information

The Supporting Information is available free of charge on the ACS Publications website at DOI: 10.1021/acsami.8b03163.

XRD patterns, SEM top view and cross section, XPS details, Arrhenius plot of conductivity, details on the calculation of conductivity, Kramers−Kronig test results, and fitting methods for Arrhenius plots (PDF)

■ AUTHOR INFORMATION

Corresponding Author

*E-mail: stephan.buecheler@empa.ch.

ORCID

M. Rawlence: 0000-0002-9475-7164

A. Remhof: 0000-0002-8394-9646

S. Buecheler: 0000-0003-0942-9965

Notes

The authors declare no competing financial interest.

■ ACKNOWLEDGMENTS

The authors acknowledge the Competence Centre for Energy and Mobility (CCEM) and Swiss Electric Research for funding the project: Proposal 911 "SLIB—All Solid State Li-Ion Batteries based on New Ceramic Li-Ion Electrolytes". T.Y.L. acknowledges financial support from Ministry of Science and Technology, Taiwan (106-2917-I-564-001-A1). The laboratory for Nanoscale Materials Science is gratefully acknowledged for granting access to the XPS measurement facilities.

■ REFERENCES

(1) Murugan, R.; Thangadurai, V.; Weppner, W. Fast Lithium Ion Conduction in Garnet-Type Li7La3Zr2O12. *Angew. Chem., Int. Ed.* **2007**, *46*, 7778−7781.

(2) Awaka, J.; Kijima, N.; Hayakawa, H.; Akimoto, J. Synthesis and Structure Analysis of Tetragonal Li7La3Zr2O12 with the Garnet-Related Type Structure. *J. Solid State Chem.* **2009**, *182*, 2046−2052.

(3) Wolfenstine, J.; Rangasamy, E.; Allen, J. L.; Sakamoto, J. High Conductivity of Dense Tetragonal Li7La3Zr2O12. *J. Power Sources* **2012**, *208*, 193−196.

(4) Awaka, J.; Takashima, A.; Kataoka, K.; Kijima, N.; Idemoto, Y.; Akimoto, J. Crystal Structure of Fast Lithium-Ion-Conducting Cubic Li7La3Zr2O12. *Chem. Lett.* **2011**, *40*, 60−62.

(5) Wagner, R.; Redhammer, G. J.; Rettenwander, D.; Senyshyn, A.; Schmidt, W.; Wilkening, M.; Amthauer, G. Crystal Structure of Garnet-Related Li-Ion Conductor Li7−3xGaxLa3Zr2O12: Fast Li-Ion Conduction Caused by a Different Cubic Modification? *Chem. Mater.* **2016**, *28*, 1861−1871.

(6) Buschmann, H.; Dolle, J.; Berendts, S.; Kuhn, A.; Bottke, P.; Wilkening, M.; Heitjans, P.; Senyshyn, A.; Ehrenberg, H.; Lotnyk, A.; Duppel, V.; Kienle, L.; Janek, J. Structure and Dynamics of the Fast Lithium Ion Conductor "Li7La3Zr2O12". *Phys. Chem. Chem. Phys.* **2011**, *13*, 19378−19392.

(7) Thangadurai, V.; Narayanan, S.; Pinzaru, D. Garnet-Type Solid-State Fast Li Ion Conductors for Li Batteries: Critical Review. *Chem. Soc. Rev.* **2014**, *43*, 4714−4727.

(8) Nemori, H.; Matsuda, Y.; Mitsuoka, S.; Matsui, M.; Yamamoto, O.; Takeda, Y.; Imanishi, N. Stability of Garnet-Type Solid Electrolyte Li(x)La(3)A(2-y)B(y)O(12) (A = Nb or Ta, B = Sc or Zr). *Solid State Ionics* **2015**, *282*, 7−12.

(9) Rettenwander, D.; Welzl, A.; Cheng, L.; Fleig, J.; Musso, M.; Suard, E.; Doeff, M. M.; Redhammer, G. J.; Amthauer, G. Synthesis, Crystal Chemistry, and Electrochemical Properties of Li(7-2x)La3Zr(2-x)Mo-(x)O12 (x = 0.1−0.4): Stabilization of the Cubic Garnet Polymorph via Substitution of Zr(4+) by Mo(6+). *Inorg. Chem.* **2015**, *54*, 10440−10449.

(10) Yan, B.; Kotobuki, M.; Liu, J. Ruthenium Doped Cubic-Garnet Structured Solid Electrolyte Li7La3Zr2-XRuxO12. *Mater. Technol.* **2016**, *31*, 623−627.

(11) Orera, A.; Larraz, G.; Alberto Rodriguez-Velamazan, J.; Campo, J.; Luisa Sanjuan, M. Influence of Li+ and H+ Distribution on the Crystal Structure of Li7-XHxLa3Zr2O12 (0 ≤ x ≤ 5) Garnets. *Inorg. Chem.* **2016**, *55*, 1324−1332.

(12) Song, S.; Sheptyakov, D.; Korsunsky, A. M.; Duong, H. M.; Lu, L. High Li Ion Conductivity in a Garnet-Type Solid Electrolyte via Unusual Site Occupation of the Doping Ca Ions. *Mater. Des.* **2016**, *93*, 232−237.

(13) Hamao, N.; Kataoka, K.; Kijima, N.; Akimoto, J. Synthesis, Crystal Structure and Conductive Properties of Garnet-Type Lithium Ion Conductor Al-Free Li7-XLa3Zr2-XTaxO12 (0 ≤ x ≤ 0.6). *J. Ceram. Soc. Jpn.* **2016**, *124*, 678−683.

(14) Rettenwander, D.; Wagner, R.; Langer, J.; Maier, M. E.; Wilkening, M.; Amthauer, G. Crystal Chemistry of "Li7La3Zr2O12" Garnet Doped with Al, Ga, and Fe: A Short Review on Local Structures as Revealed by NMR and Mossbauer Spectroscopy Studies. *Eur. J. Mineral.* **2016**, *28*, 619−629.

(15) Deviannapoorani, C.; Shankar, L. S.; Ramakumar, S.; Murugan, R. Investigation on Lithium Ion Conductivity and Structural Stability of Yttrium-Substituted Li7La3Zr2O12. *Ionics* **2016**, *22*, 1281−1289.

(16) Cai, L.; Zhao-Yin, W.; Kun, R. High Ion Conductivity in Garnet-Type F-Doped Li7La3Zr2O12. *J. Inorg. Mater.* **2015**, *30*, 995−1000.

(17) Li, Y.; Wang, Z.; Cao, Y.; Du, F.; Chen, C.; Cui, Z.; Guo, X. W-Doped Li7La3Zr2O12 Ceramic Electrolytes for Solid State Li-Ion Batteries. *Electrochim. Acta* **2015**, *180*, 37−42.

(18) Hanc, E.; Zajac, W.; Molenda, J. Synthesis Procedure and Effect of Nd, Ca and Nb Doping on Structure and Electrical Conductivity of Li7La3Zr2O12 Garnets. *Solid State Ionics* **2014**, *262*, 617−621.

(19) Matsuda, Y.; Itami, Y.; Hayamizu, K.; Ishigaki, T.; Matsui, M.; Takeda, Y.; Yamamoto, O.; Imanishi, N. Phase Relation, Structure and Ionic Conductivity of Li7-x-3yAlyLa3Zr2-XTaxO12. *RSC Adv.* **2016**, *6*, 78210−78218.

(20) Rettenwander, D.; Redhammer, G.; Preishuber-Pflügl, F.; Cheng, L.; Miara, L.; Wagner, R.; Welzl, A.; Suard, E.; Doeff, M. M.; Wilkening,

DOI: 10.1021/acsami.8b03163
ACS Appl. Mater. Interfaces 2018, 10, 13720−13728

M.; Fleig, j; Amthauer, G. Structural and Electrochemical Consequences of Al and Ga Cosubstitution in Li7La3Zr2O12 Solid Electrolytes. *Chem. Mater.* **2016**, *28*, 2384−2392.

(21) Shin, D. O.; Oh, K.; Kim, K. M.; Park, K.-Y.; Lee, B.; Lee, Y.-G.; Kang, K. Synergistic Multi-Doping Effects on the Li7La3Zr2O12 Solid Electrolyte for Fast Lithium Ion Conduction. *Sci. Rep.* **2015**, *5*, No. 18053.

(22) Cao, Z.; Cao, X.; Liu, X.; He, W.; Gao, Y.; Liu, J.; Zeng, J. Effect of Sb-Ba Co-Doping on the Ionic Conductivity of Li7La3Zr2O12 Ceramic. *Ceram. Int.* **2015**, *41*, 6232−6236.

(23) Gu, W.; Ezbiri, M.; Prasada Rao, R.; Avdeev, M.; Adams, S. Effects of Penta- and Trivalent Dopants on Structure and Conductivity of Li7La3Zr2O12. *Solid State Ionics* **2015**, *274*, 100−105.

(24) Tong, X.; Thangadurai, V.; Wachsman, E. D. Highly Conductive Li Garnets by a Multielement Doping Strategy. *Inorg. Chem.* **2015**, *54*, 3600−3607.

(25) Dhivya, L.; Murugan, R. Effect of Simultaneous Substitution of Y and Ta on the Stabilization of Cubic Phase, Microstructure, and Li+ Conductivity of Li7La3Zr2O12 Lithium Garnet. *ACS Appl. Mater. Interfaces* **2014**, *6*, 17606−17615.

(26) Wu, J.-F.; Chen, E.-Y.; Yu, Y.; Liu, L.; Wu, Y.; Pang, W. K.; Peterson, V. K.; Guo, X. Gallium-Doped Li7La3Zr2O12 Garnet-Type Electrolytes with High Lithium-Ion Conductivity. *ACS Appl. Mater. Interfaces* **2017**, *9*, 1542−1552.

(27) Bernuy-Lopez, C.; Manalastas, W.; del Amo, J. M. L.; Aguadero, A.; Aguesse, F.; Kilner, J. A. Atmosphere Controlled Processing of Ga-Substituted Garnets for High Li-Ion Conductivity Ceramics. *Chem. Mater.* **2014**, *26*, 3610−3617.

(28) Afyon, S.; Krumeich, F.; Rupp, J. L. M. A Shortcut to Garnet-Type Fast Li-Ion Conductors for All-Solid State Batteries. *J. Mater. Chem. A* **2015**, *3*, 18636−18648.

(29) Wagner, R.; Redhammer, G. J.; Rettenwander, D.; Tippelt, G.; Welzl, A.; Taibl, S.; Fleig, J.; Franz, A.; Lottermoser, W.; Amthauer, G. Fast Li-Ion-Conducting Garnet-Related Li7-3xFexLa3Zr2O12 with Uncommon I(4)over-Bar3d Structure. *Chem. Mater.* **2016**, *28*, 5943−5951.

(30) Thompson, T.; Yu, S.; Williams, L.; Schmidt, R. D.; Garcia-Mendez, R.; Wolfenstine, J.; Allen, J. L.; Kioupakis, E.; Siegel, D. J.; Sakamoto, J. Electrochemical Window of the Li-Ion Solid Electrolyte Li7La3Zr2O12. *ACS Energy Lett.* **2017**, *2*, 462−468.

(31) Luo, W.; Gong, Y.; Zhu, Y.; Fu, K. K.; Dai, J.; Lacey, S. D.; Wang, C.; Liu, B.; Han, X.; Mo, Y.; Wachsman, E. D.; Hu, L. Transition from Superlithiophobicity to Superlithiophilicity of Garnet Solid-State Electrolyte. *J. Am. Chem. Soc.* **2016**, *138*, 12258−12262.

(32) Han, X.; Gong, Y.; Fu, K. K.; He, X.; Hitz, G. T.; Dai, J.; Pearse, A.; Liu, B.; Wang, H.; Rubloff, G.; Mo, Y.; Thangadurai, V.; Wachsman, E. D.; Hu, L. Negating Interfacial Impedance in Garnet-Based Solid-State Li Metal Batteries. *Nat. Mater.* **2017**, 572−579.

(33) Younesi, R.; Veith, G. M.; Johansson, P.; Edstrom, K.; Vegge, T. Lithium Salts for Advanced Lithium Batteries: Li-Metal, Li-O2, and Li-S. *Energy Environ. Sci.* **2015**, *8*, 1905−1922.

(34) van den Broek, J.; Afyon, S.; Rupp, J. L. M. Interface-Engineered All-Solid-State Li-Ion Batteries Based on Garnet-Type Fast Li+ Conductors. *Adv. Energy Mater.* **2016**, *6*, No. 1600736.

(35) Kato, T.; Hamanaka, T.; Yamamoto, K.; Hirayama, T.; Sagane, F.; Motoyama, M.; Iriyama, Y. In-Situ Li7La3Zr2O12/LiCoO2 Interface Modification for Advanced All-Solid-State Battery. *J. Power Sources* **2014**, *260*, 292−298.

(36) Okada, K.; Machida, N.; Naito, M.; Shigematsu, T.; Ito, S.; Fujiki, S.; Nakano, M.; Aihara, Y. Preparation and Electrochemical Properties of LiAlO2-Coated Li(Ni1/3Mn1/3Co1/3)O2 for All-Solid-State Batteries. *Solid State Ionics* **2014**, *255*, 120−127.

(37) Kim, S.; Hirayama, M.; Taminato, S.; Kanno, R. Epitaxial Growth and Lithium Ion Conductivity of Lithium-Oxide Garnet for an All Solid-State Battery Electrolyte. *Dalton Trans.* **2013**, *42*, 13112−13117.

(38) Tan, J. J.; Tiwari, A. Fabrication and Characterization of Li7La3Zr2O12 Thin Films for Lithium Ion Battery. *ECS Solid State Lett.* **2012**, *1*, Q57−Q60.

(39) Rawlence, M.; Garbayo, I.; Buecheler, S.; Rupp, J. L. M. On the Chemical Stability of Post-Lithiated Garnet Al-Stabilized Li7La3Zr2O12 Solid State Electrolyte Thin Films. *Nanoscale* **2016**, *8*, 14746−14753.

(40) Park, J. S.; Cheng, L.; Zorba, V.; Mehta, A.; Cabana, J.; Chen, G. Y.; Doeff, M. M.; Richardson, T. J.; Park, J. H.; Son, J. W.; Hong, W. S. Effects of Crystallinity and Impurities on the Electrical Conductivity of Li-La-Zr-O Thin Films. *Thin Solid Films* **2015**, *576*, 55−60.

(41) Garbayo, I.; Struzik, M.; Pfenninger, R.; Bowman, W.; Rupp, J. L. M.; et al. Glass-Type Polyamorphism in Li-Garnet Thin Film Solid State Battery Conductors. *Adv. Energy Mater.* **2017**, No. 1702265.

(42) Kalita, D. J.; Lee, S. H.; Lee, K. S.; Ko, D. H.; Yoon, Y. S. Ionic Conductivity Properties of Amorphous Li-La-Zr-O Solid Electrolyte for Thin Film Batteries. *Solid State Ionics* **2012**, *229*, 14−19.

(43) Lobe, S.; Dellen, C.; Finsterbusch, M.; Gehrke, H. G.; Sebold, D.; Tsai, C. L.; Uhlenbruck, S.; Guillon, O. Radio Frequency Magnetron Sputtering of Li7La3Zr2O12 Thin Films for Solid-State Batteries. *J. Power Sources* **2016**, *307*, 684−689.

(44) Ahn, C.-W.; Choi, J. J.; Ryu, J.; Hahn, B. D.; Kim, J. W.; Yoon, W. H.; Choi, J. H.; Park, D. S. Microstructure and Ionic Conductivity in Li7La3Zr2O12 Film Prepared by Aerosol Deposition Method. *J. Electrochem. Soc.* **2015**, *162*, A60−A63.

(45) Tadanaga, K.; Egawa, H.; Hayashi, A.; Tatsumisago, M.; Mosa, J.; Aparicio, M.; Duran, A. Preparation of Lithium Ion Conductive Al-Doped Li7La3Zr2O12 Thin Films by a Sol-Gel Process. *J. Power Sources* **2015**, *273*, 844−847.

(46) Chen, R.-J.; Huang, M.; Huang, W.-Z.; Shen, Y.; Lin, Y.-H.; Nan, C.-W. Sol-Gel Derived Li-La-Zr-O Thin Films as Solid Electrolytes for Lithium-Ion Batteries. *J. Mater. Chem. A* **2014**, *2*, 13277−13282.

(47) Bitzer, M.; Van Gestel, T.; Uhlenbruck, S.; Buchkremer, H.-P. Sol-Gel Synthesis of Thin Solid Li7La3Zr2O12 Electrolyte Films for Li-Ion Batteries. *Thin Solid Films* **2016**, *615*, 128−134.

(48) Katsui, H.; Goto, T. Preparation of Cubic and Tetragonal Li7La3Zr2O12 Film by Metal Organic Chemical Vapor Deposition. *Thin Solid Films* **2015**, *584*, 130−134.

(49) Langer, F.; Glenneberg, J.; Bardenhagen, I.; Kun, R. Synthesis of Single Phase Cubic Al-Substituted Li7La3Zr2O12 by Solid State Lithiation of Mixed Hydroxides. *J. Alloys Compd.* **2015**, *645*, 64−69.

(50) Chen, R.-J.; Huang, M.; Huang, W.-Z.; Shen, Y.; Lin, Y.-H.; Nan, C.-W. Effect of Calcining and Al Doping on Structure and Conductivity of Li7La3Zr2O12. *Solid State Ionics* **2014**, *265*, 7−12.

(51) Cheng, L.; Wu, C. H.; Jarry, A.; Chen, W.; Ye, Y.; Zhu, J.; Kostecki, R.; Persson, K.; Guo, J.; Salmeron, M.; Chen, G.; Doeff, M. Interrelationships among Grain Size, Surface Composition, Air Stability, and Interfacial Resistance of Al-Substituted Li7La3Zr2O12 Solid Electrolytes. *ACS Appl. Mater. Interfaces* **2015**, *7*, 17649−17655.

(52) Matsui, M.; Takahashi, K.; Sakamoto, K.; Hirano, A.; Takeda, Y.; Yamamoto, O.; Imanishi, N. Phase Stability of a Garnet-Type Lithium Ion Conductor Li7La3Zr2O12. *Dalton Trans.* **2014**, *43*, 1019−1024.

(53) Lotgering, F. K. Topotactical Reactions with Ferrimagnetic Oxides Having Hexagonal Crystal Structures—I. *J. Inorg. Nucl. Chem.* **1959**, *9*, 113−123.

(54) Howard, M. A.; Clemens, O.; Kendrick, E.; Knight, K. S.; Apperley, D. C.; Anderson, P. A.; Slater, P. R. Effect of Ga Incorporation on the Structure and Li Ion Conductivity of La3Zr2Li7O12. *Dalton Trans.* **2012**, *41*, 12048−12053.

(55) Kubicek, M.; Wachter-Welz, A.; Rettenwander, D.; Wagner, R.; Berendts, S.; Uecker, R.; Anathauer, G.; Hutter, H.; Fleig, J. Oxygen Vacancies in Fast Lithium-Ion Conducting Garnets. *Chem. Mater.* **2017**, *29*, 7189−7196.

(56) Toll, J. S. Causality and the Dispersion Relation: Logical Foundations. *Phys. Rev.* **1956**, *104*, 1760−1770.

(57) Habasaki, J.; Leon, C.; Ngai, K. L. *Dynamics of Glassy, Crystalline and Liquid Ionic Conductors*; Topics in Applied Physics; Springer, 2017; Vol. *132*.

(58) León, C.; Santamaría, J.; París, M. A.; Sanz, J.; Ibarra, J.; Torres, L. M. Non-Arrhenius Conductivity in the Fast Ionic Conductor Li(0.5)-La(0.5)TiO(3) Reconciling Spin-Lattice and Electrical-Conductivity Relaxations. *Phys. Rev. B* **1997**, *56*, 5302−5305.

DOI: 10.1021/acsami.8b03163
ACS Appl. Mater. Interfaces 2018, 10, 13720−13728